Phase Characterization of (Mn, S) inclusions and Mo precipitates within reactor pressure vessel steel from Greifswald Nuclear Power Plant

Ghada Yassin, Erik Pönitz, Nina Maria Huittinen, Dieter Schild, Jörg Konheiser, Katharina Müller, Astrid Barkleit*

Supporting Information

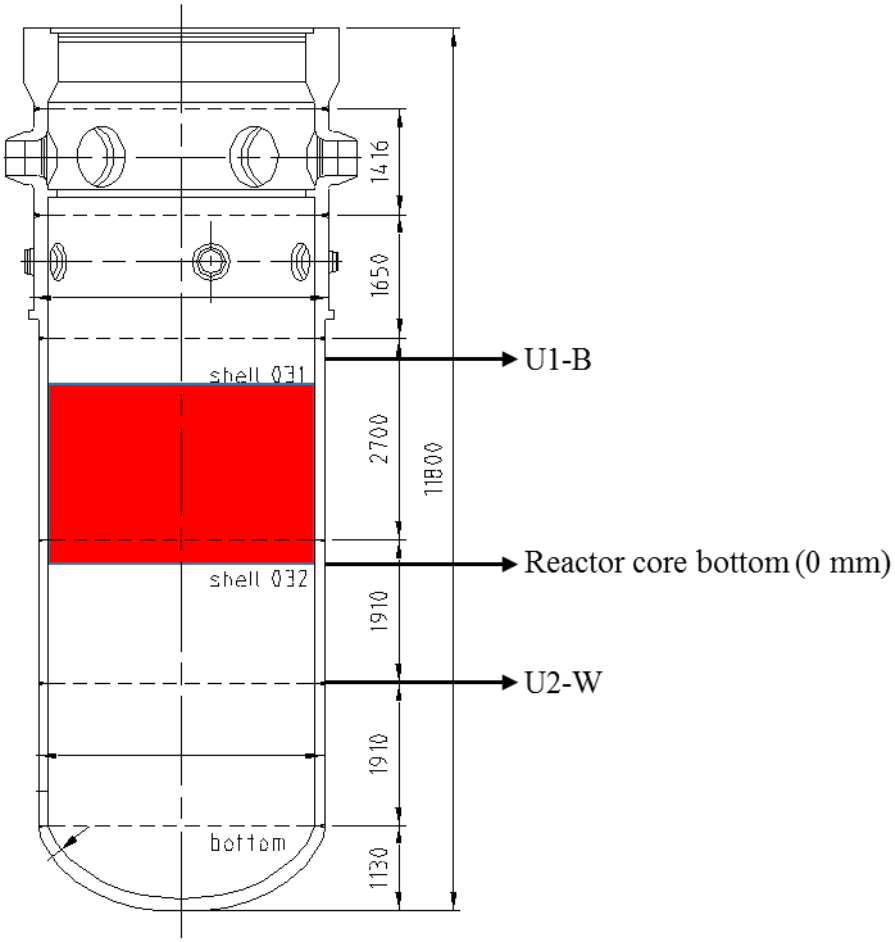


Figure S1. Schematic of the sampling positions of trepans taken from RPV of Greifswald-NPP that were in-operandi representing U1-B, taken at 275 cm and U2-W, taken at –161 cm from the reactor core bottom as reference (after [1]).

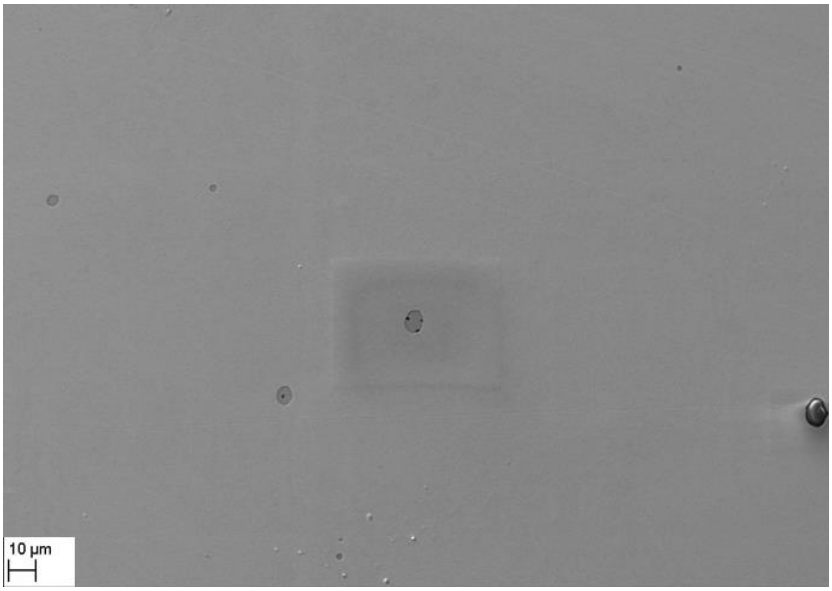


Figure S2. SEM imaging of the first generation reactor units sample U1-B, revealing the presence of dark areas of (Mn, S) enriched inclusions and the presence of Mo bright precipitates.

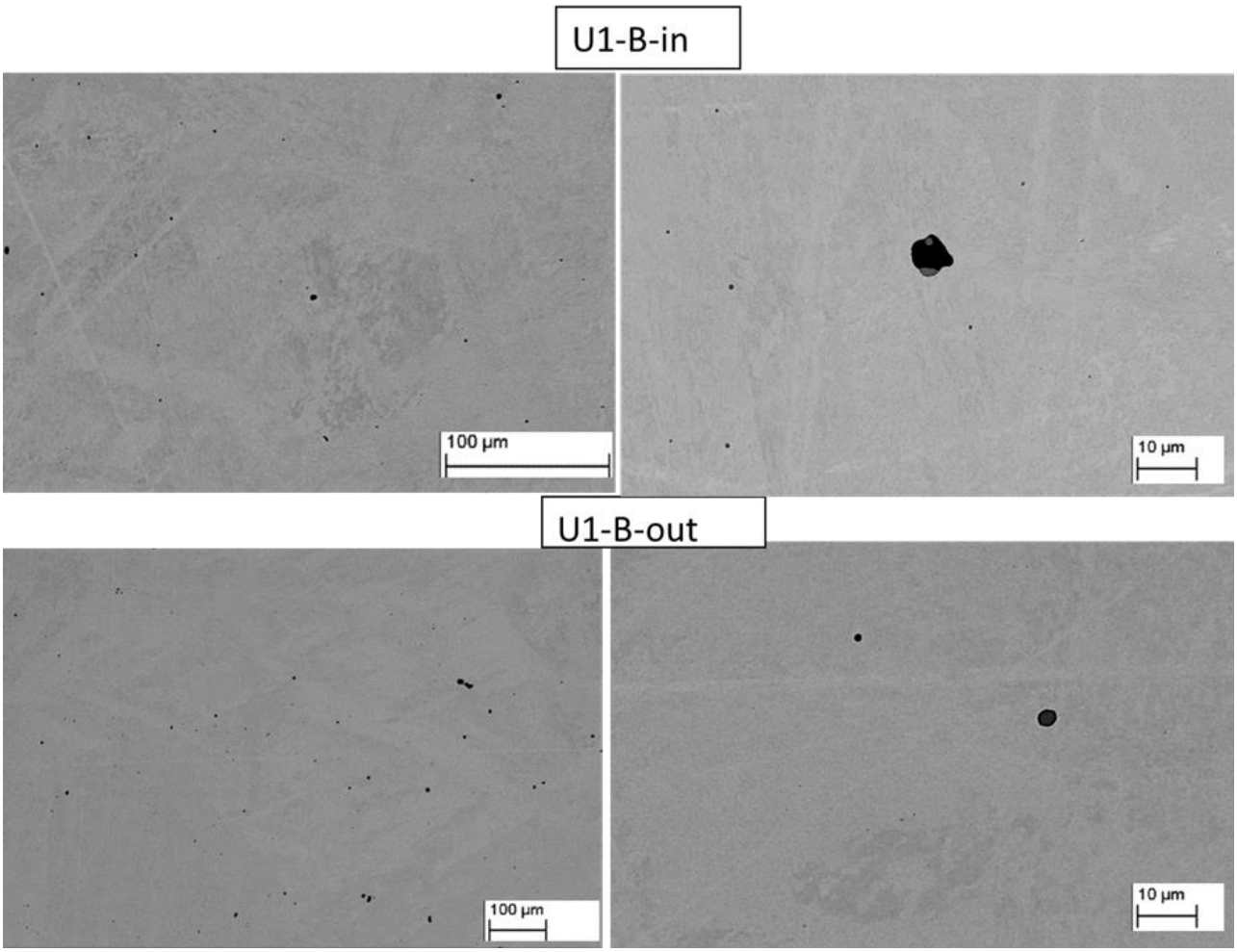


Figure S3. Microstructural features of base metal samples U1-B showing the distribution of (Mn, S) inclusions within the matrix, with different size dimensions within the range of *ca.* (6-9) µm.

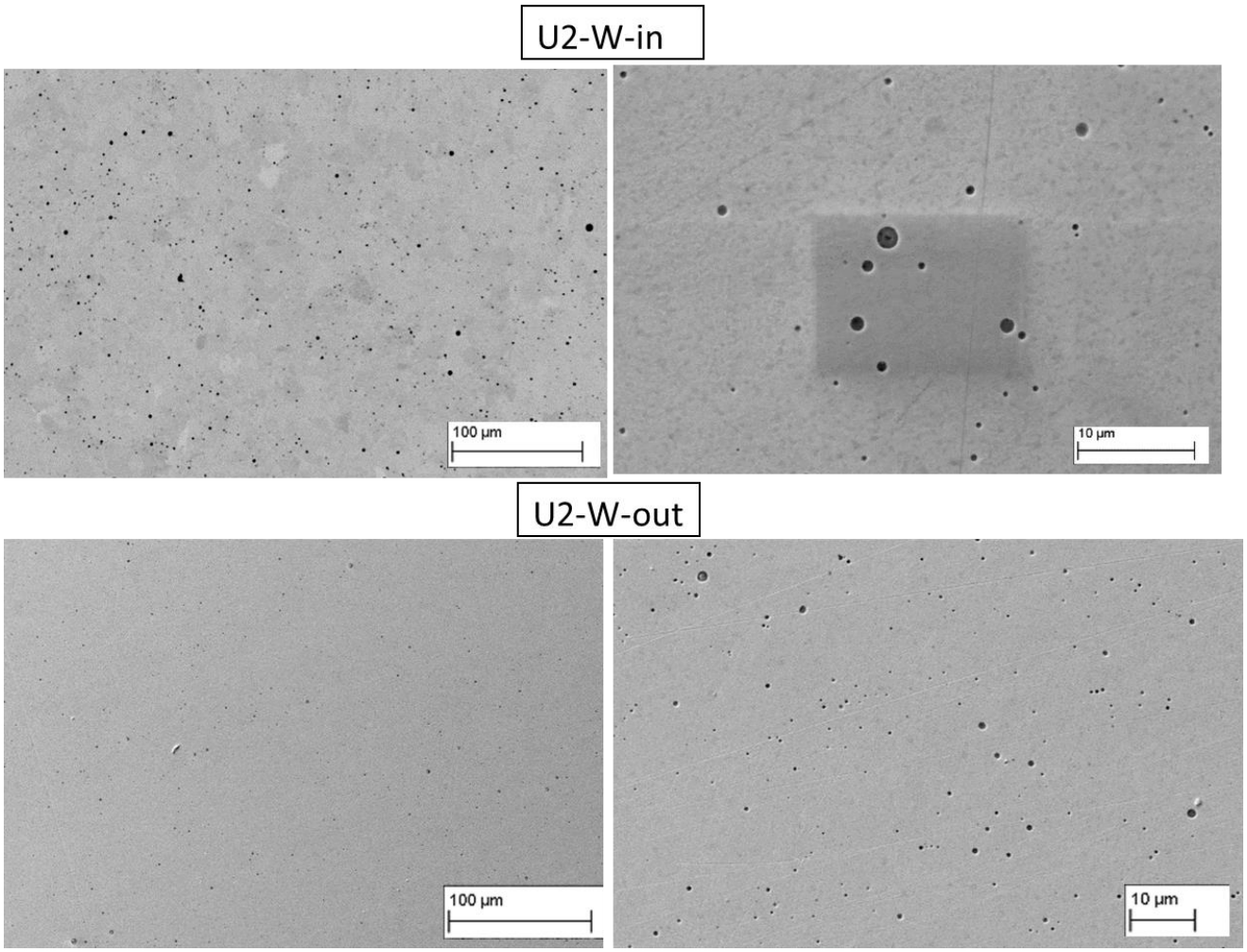


Figure S4. Microstructural features of the weld metal samples U2-W showing more homogeneous distribution of (Mn, S) inclusion, with smaller size within the range from *ca.* (1µ m to 90 nm) compared to U1-B.

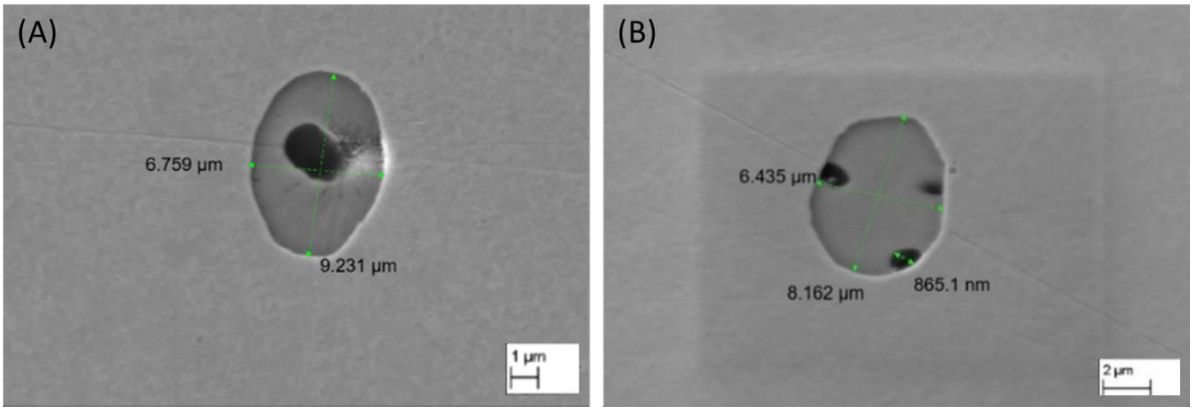


Figure S5. (Mn, S) inclusions within the first generation base material of U1-B within A) the inner wall and B) outer wall of the RPV with average size of the inclusions (6-9) µm and their secondary micro-inclusions of average size of 865 nm.

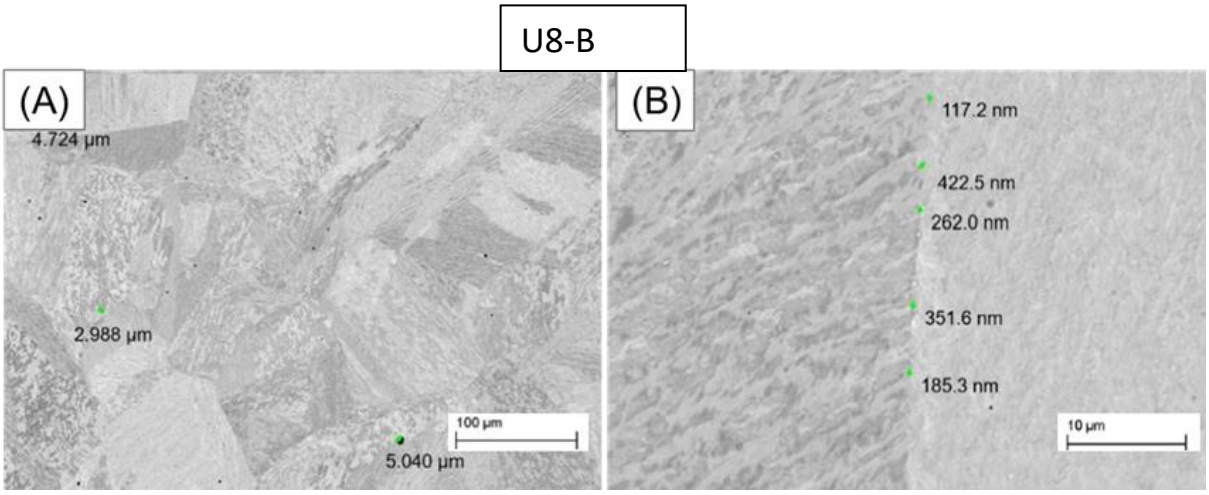


Figure S6. Backscattered electron imaging of RPV steel material of U8-B showing (A) the (Mn, S) inclusions at different locations with size range (1 µm -10 µm) level, (B) Mo-precipitates of size range of *ca.* 100 nm on their boundaries.

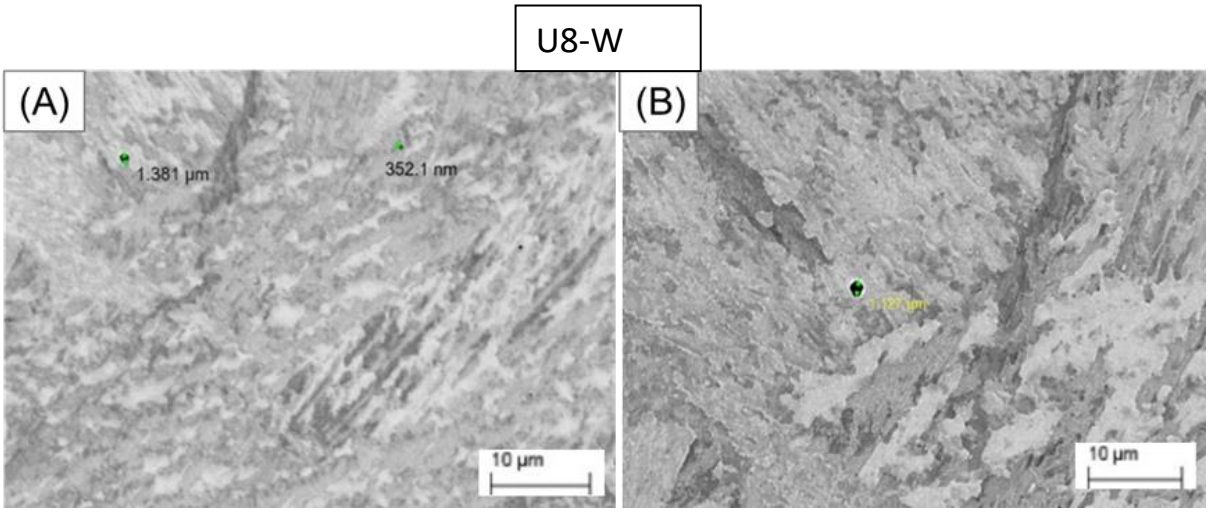


Figure S7. Backscattered electron imaging of the weld RPV material (U8-W) showing the distribution of the (Mn, S) inclusions with small size range (nm-µm) at different locations.

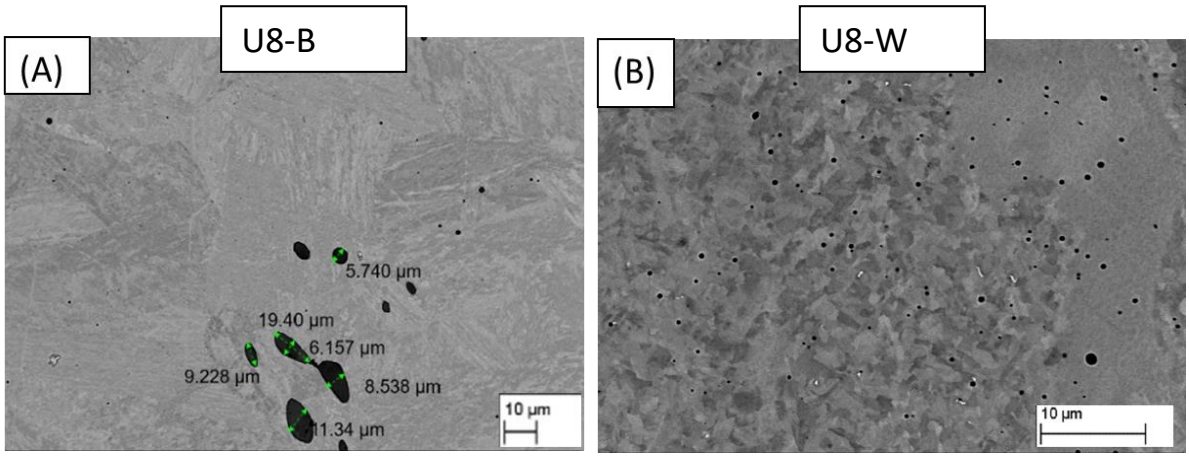


Figure S8. Microstructural features U8-B (left) with (Mn, S)-inclusion of size range up to 20µm material, indicating that the material might undergo inhomogeneity of the composition mixture at certain locations; and U8-W (right) with more homogenous distributed inclusions.

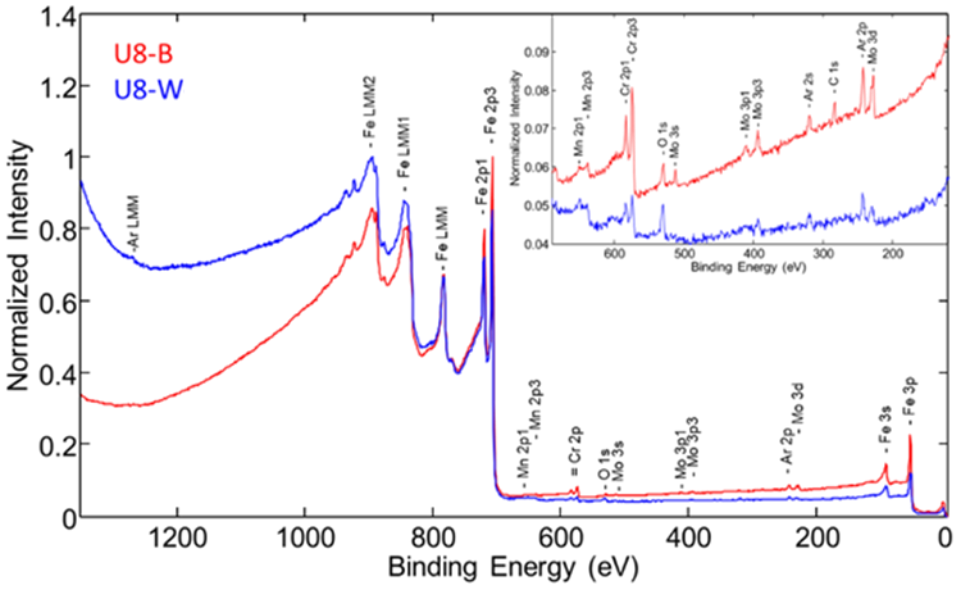


Figure S9. XPS survey of base (U8-B) and weld (U8-W) samples.

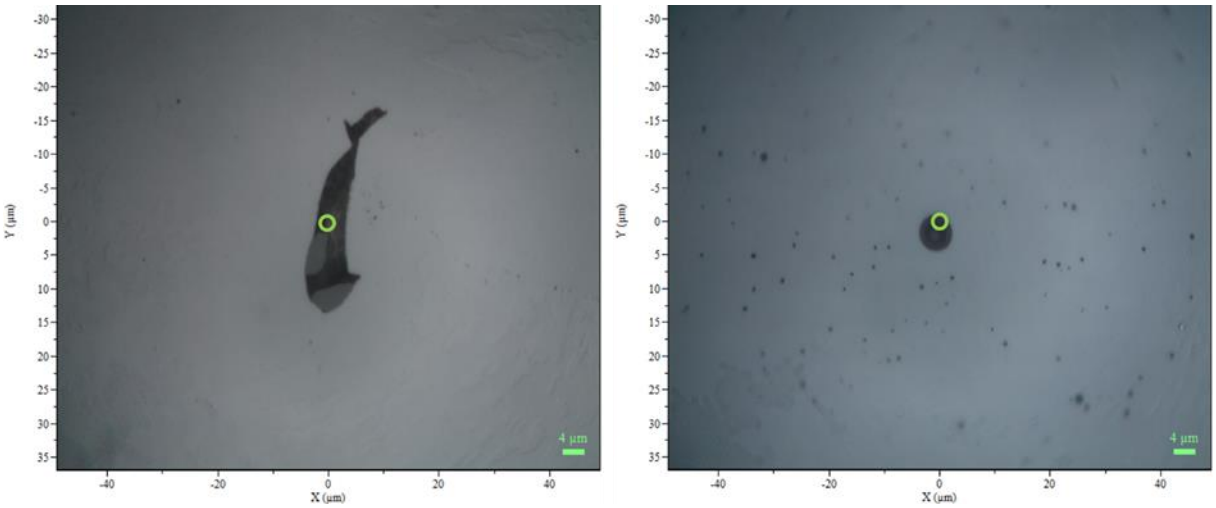


Figure S10. Optical image with indication of area analyzed by Raman spectroscopy of the laser spots taken within the (Mn, S)-rich inclusions of the second generation samples; base sample U8-B (left) and the weld sample U8-W(right). The length of the scale bar (bottom right in green each) represents 4 µm.

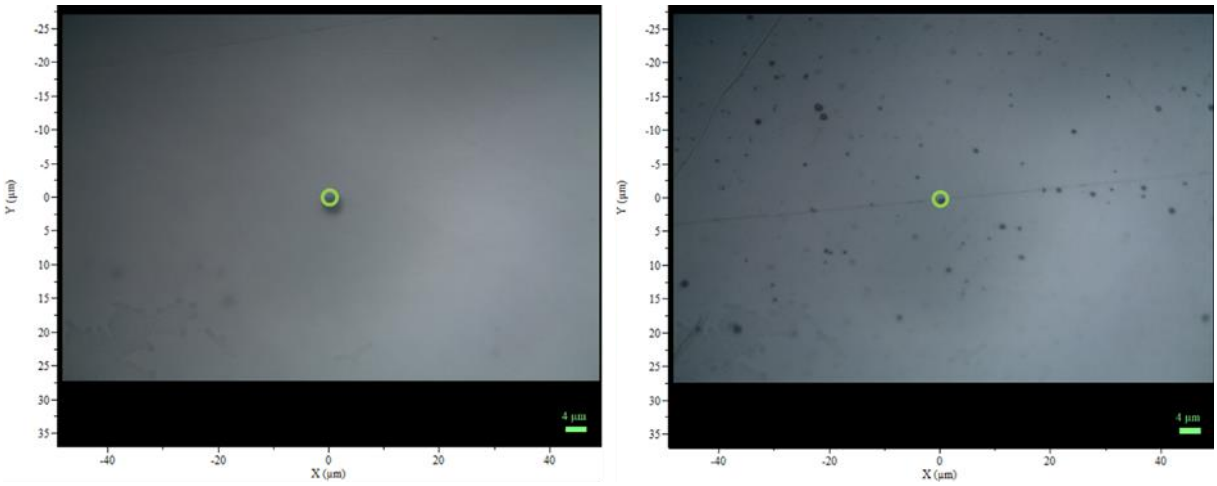


Figure S11. Optical image with indication of area analyzed by Raman spectroscopy of the laser spot taken within the (Mn, S)-inclusion of the first generation samples; of the base (U1-B, left) and the weld material (U2-W, right). The length of the scale bar (bottom right in green each) represents 4 µm.

Table S1. Summary of Raman bands from literature.

Compound	Raman bands (cm^{-1})	Laser	Reference
MnS	**635** (s)	514 nm	[2]
	355 (w), **637** (s)	514 nm	[3]
	350 (w), **650** (s)	?	[4]
(Fe,Mn)S	**276** (s), 314 (m)	532 nm	[5]
FeS (mackinawite)	**282** (m)	532 nm	[5]
	216 (s), **278** (s), **390** (m)	532 nm	[6]
	207 (w), 254 (w), **296** (s)	633 nm	[7]
Fe_3S_4 (greigite)	**342** (s)	532 nm	[5]
	188 (w), 250 (w), **351** (s), 366 (w, sh)	633 nm	[7]
S	**154** (s), **221** (s), 437 (w), **474** (s)	532 nm	[6]
Fe_3O_4 (magnetite)	292 (w), 524 (w), **665** (s)	647 nm	[8]
	350 (w), 535 (w), **672** (s)	514 nm	[9]
	665 (s)	532 nm	[10]
α-Fe_2O_3 (hematite)	**224** (s), 243 (w), **290** (s), 406 (m), 494 (w), 607 (w), 1310 (m, br)	647 nm	[8]
	220 (m), 280 (m), 400 (w)	532 nm	[11]
γ-Fe_2O_3 (Maghemite)	290 (w), **339** (s), **378** (s), **507** (s), 575 (w), **630** (s), **657** (s), **723** (s), 1417 (m, br)	647 nm	[8]
NiO	**480** (s, br)	532 nm	[12]
Cr_2O_3	**350** (s), 527 (w), **552** (s), **613** (s)	647 nm	[13]
	302 (w), 347 (w), **550** (s), 608 (w)	532 nm	[12]
$NiFe_2O_4$	325 (w, br), **455** (s), 488 (sh), 565 (w), 650 (sh), **695** (s)	532 nm	[12]
	488 (m), 570 (m), 592 (m), **705** (s)	647 nm	[14]
$NiCr_2O_4$	430 (w), **514** (s), 685 (w)	647 nm	[14]
	425 (m), 508 (s), 549 (m), **665** (s)	532 nm	[12]
$MnFe_2O_4$	340 (w), 456 (w) 563 (w), **646** (s)	532 nm	[15]
	643 (s)	532 nm	[5]
silicate	~**960-1050** (s, br)	?	[16]
	770 (m), **~1000** (s)	633 nm	[17]
	330 (m), 654 (m), **674 (669)** (s), **1003 (1005)** (s)	532 nm	[6]
s … strong, m … medium, w … weak; br … broad, sh … shoulder			

References

1. Rindelhardt, U., Viehrig, H.W., Konheiser, J., Schuhknecht, J., Noack, K. and Gleisberg, B., *RPV material investigations of the former VVER-440 Greifswald NPP*. Nuclear Engineering and Design, 2009. **239**(9): 1581-1590. DOI: 10.1016/j.nucengdes.2008.07.018.
2. Alanazi, A.M., McNaughter, P.D., Alam, F., Vitorica-yrezabal, I.J., Whitehead, G.F.S., Tuna, F., O'Brien, P., Collison, D. and Lewis, D.J., *Structural Investigations of alpha-MnS Nanocrystals and Thin Films Synthesized from Manganese(II) Xanthates by Hot Injection, Solvent-Less Thermolysis, and Doctor Blade Routes.* Acs Omega, 2021. **6**(42): 27716-27725. DOI: 10.1021/acsomega.1c02907.

3. Girish, M., Dhandayuthapani, T., Sivakumar, R. and Sanjeeviraja, C., *MnS thin films prepared by a simple and novel nebulizer technique: report on the structural, optical, and dispersion energy parameters.* Journal of Materials Science-Materials in Electronics, 2015. **26**(6): 3670-3684. DOI: 10.1007/s10854-015-2885-7.
4. Ramki, S., Pandi, K., Chen, S.M., Ye, Y.T., Chen, T.W. and Hao, Q.L., *Hydrothermal Synthesis of Manganese Sulfide Decorated Graphene Oxide for Effective Electrochemical Sensing of Dopamine.* International Journal of Electrochemical Science, 2019. **14**(1): 1069-1081. DOI: 10.20964/2019.01.58.
5. Li, S.X. and Hihara, L.H., *Identification of inclusions in carbon steels using micro-Raman spectroscopy.* Journal of Raman Spectroscopy, 2017. **48**(1): 137-142. DOI: 10.1002/jrs.4993.
6. Huidobro, J., Aramendia, J., Garcia-Florentino, C., Ruiz-Galende, P., Torre-Fdez, I., Castro, K., Arana, G. and Madariaga, J.M., *Mineralogy of the RBT 04262 Martian meteorite as determined by micro-Raman and micro-X-ray fluorescence spectroscopies.* Journal of Raman Spectroscopy, 2022. **53**(3): 450-462. DOI: 10.1002/jrs.6291.
7. Bourdoiseau, J.A., Jeannin, M., Remazeilles, C., Sabota, R. and Refait, P., *The transformation of mackinawite into greigite studied by Raman spectroscopy.* Journal of Raman Spectroscopy, 2011. **42**(3): 496-504. DOI: 10.1002/jrs.2729.
8. Maslar, J.E., Hurst, W.S., Bowers, W.J., Hendricks, J.H. and Aquino, M.I., *In situ Raman spectroscopic investigation of aqueous iron corrosion at elevated temperatures and pressures.* Journal of the Electrochemical Society, 2000. **147**(7): 2532-2542. DOI: 10.1149/1.1393565.
9. Molchan, I.S., Thompson, G.E., Lindsay, R., Skeldon, P., Likodimos, V., Romanos, G.E., Falaras, P., Adamova, G., Iliev, B. and Schubert, T.J.S., *Corrosion behaviour of mild steel in 1-alkyl-3-methylimidazolium tricyanomethanide ionic liquids for CO_2 capture applications.* Rsc Advances, 2014. **4**(11): 5300-5311. DOI: 10.1039/c3ra45872e.
10. Kim, J., Kim, S.H., Choi, K.J., Bahn, C.B., Hwang, I.S. and Kim, J.H., *In-situ investigation of thermal aging effect on oxide formation in Ni-base alloy/low alloy steel dissimilar metal weld interfaces.* Corrosion Science, 2014. **86**: 295-303. DOI: 10.1016/j.corsci.2014.06.006.
11. Dywel, P., Szczesny, R., Domanowski, P. and Skowronski, L., *Structural and Micromechanical Properties of Nd:YAG Laser Marking Stainless Steel (AISI 304 and AISI 316).* Materials, 2020. **13**(9): 14. DOI: 10.3390/ma13092168.
12. Kim, J., Choi, K.J., Bahn, C.B. and Kim, J.H., *In situ Raman spectroscopic analysis of surface oxide films on Ni-base alloy/low alloy steel dissimilar metal weld interfaces in high-temperature water.* Journal of Nuclear Materials, 2014. **449**(1-3): 181-187. DOI: 10.1016/j.jnucmat.2014.03.038.
13. Maslar, J.E., Hurst, W.S., Bowers, W.J., Hendricks, J.H., Aquino, M.I. and Levin, I., *In situ Raman spectroscopic investigation of chromium surfaces under hydrothermal conditions.* Applied Surface Science, 2001. **180**(1-2): 102-118. DOI: 10.1016/s0169-4332(01)00338-5.
14. Maslar, J.E., Hurst, W.S., Bowers, W.J. and Hendricks, J.H., *In situ Raman spectroscopic investigation of stainless steel hydrothermal corrosion.* Corrosion, 2002. **58**(9): 739-747. DOI: 10.5006/1.3277656.
15. Rafique, M.Y., Pan, L.Q., Javed, Q.U., Iqbal, M.Z., Qiu, H.M., Farooq, M.H., Guo, Z.G. and Tanveer, M., *Growth of monodisperse nanospheres of $MnFe_2O_4$ with enhanced magnetic and optical properties.* Chinese Physics B, 2013. **22**(10): 7. DOI: 10.1088/1674-1056/22/10/107101.

16. He, X.B., Wang, L.J. and Chou, K.C., *Basicity Contributions to Interfacial Structure and Oxygen Potential of CaO-MnO-SiO_2 slag.* Metallurgical and Materials Transactions B-Process Metallurgy and Materials Processing Science, 2022. **53**(3): 1583-1592. DOI: 10.1007/s11663-022-02467-9.
17. Takahashi, N., Tsujimori, T., Kamada, S. and Nakamura, M., *In-situ Raman spectroscopic analysis of dissolved silica structures in Na_2CO_3 and NaOH solutions at high pressure and temperature.* Contributions to Mineralogy and Petrology, 2022. **177**(3): 15. DOI: 10.1007/s00410-022-01892-y.